Structural Engineering and Mechanics, Vol. 13, No. 6 (2002) 615-638 615
DOI: http://dx.doi.org/10.12989/sem.2002.13.6.615

Fluid-structure-soil interaction analysis of cylindrical liquid storage tanks subjected to horizontal earthquake loading

Jae-Min Kim†

Department of Ocean Civil Engineering, Yosu National University, Yosu, Chonnam 550-749, Korea

Soo-Hyuk Chang‡ and Chung-Bang Yun‡†

Department of Civil Engineering, Korea Advanced Institute of Science & Technology, Daejeon 305-701, Korea

(Received February 28, 2000, Revised July 12, 2001, Accepted March 7, 2002)

Abstract. This paper presents a method of seismic analysis for a cylindrical liquid storage structure considering the effects of the interior fluid and exterior soil medium in the frequency domain. The horizontal and rocking motions of the structure are included in this study. The fluid motion is expressed in terms of analytical velocity potential functions, which can be obtained by solving the boundary value problem including the deformed configuration of the structure as well as the sloshing behavior of the fluid. The effect of the fluid is included in the equation of motion as the impulsive added mass and the frequency-dependent convective added mass along the nodes on the wetted boundary of the structure. The structure and the near-field soil medium are represented using the axisymmetric finite elements, while the far-field soil is modeled using dynamic infinite elements. The present method can be applied to the structure embedded in ground as well as on ground, since it models both the soil medium and the structure directly. For the purpose of verification, earthquake response analyses are performed on several cases of liquid tanks on a rigid ground and on a homogeneous elastic half-space. Comparison of the present results with those by other methods shows good agreement. Finally, an application example of a reinforced concrete tank on a horizontally layered soil with a rigid bedrock is presented to demonstrate the importance of the soil-structure interaction effects in the seismic analysis for large liquid storage tanks.

Key words: cylindrical liquid storage tank; fluid-structure-soil interaction; added mass; infinite element; velocity potential; earthquake response analysis.

1. Introduction

The cylindrical shell of revolution is the most popular type of structure for a liquid storage tank. The large-scale liquified natural gas(LNG) tank is one of those, of which diameter is in the order of

† Assistant Professor
‡ Graduate Research Assistant
‡† Professor

70 m and height is about 60 m. For the safety of the structure, a very strong and massive containment structure is usually needed, which usually makes the structural system vulnerable to seismic excitation. Therefore, base-isolation systems have been often applied to the structures when constructed on ground. Otherwise, they are embedded in ground to reduce the seismic influence.

The hydrodynamic interaction of the contained liquid with the structure can be considered as the impulsive and convective pressure loads exerted on the wetted interface during ground excitations like a dynamic earthquake loads. The impulsive component represents the mass of the liquid moving together with the structure, while the convective one reflects the effects of the free surface sloshing. Based on various theoretical developments, tests in laboratories, and observations on actual behavior of the structure during earthquake events, practical seismic design procedures have been established for the up-right thin cylindrical liquid storage tank which is either anchored or unanchored on the rigid ground (Housner 1963, Balendra *et al.* 1982, Haroun 1983).

The effect of the soil flexibility on the fluid-structure interaction has been studied by many researchers and engineers, since the seismic analysis assuming a rigid ground condition often gives overly conservative results. Several works relevant to the effects of the supporting soil are those by Veletsos and Tang (1990), Hori (1990), Natsiavas (1990), Seebar *et al.* (1990), and Haroun and Abou-Izzeddine (1992). They employed the discrete finite element method or continuous potential functions to model the fluid region, while the soil is represented by a substructured frequency-dependent impedance matrix associated with the rigid-body motion of the foundation. Conclusions from the studies were that the flexibility of the soil medium is substantially important for the dynamic analysis of the structure, and the results may highly depend on the soil conditions as well as the configuration of the structure. Accordingly, it has been required to develop a versatile and accurate methodology, which can directly deal with the complex system with the same emphasis on both soil-structure interaction and fluid-structure interaction, to achieve economical as well as safe structural design.

This paper presents a fully coupled fluid-structure-soil interaction analysis technique for cylindrical liquid-contained structures subjected to horizontal ground excitation. For this purpose, a new closed-form velocity potential solution is derived for the motion of the liquid subjected to the horizontal and rocking excitations with consideration of the structural flexibility and the free-surface sloshing. The hydrodynamic forces on the structure are incorporated as a frequency dependent added mass matrix along the wetted boundary. The axisymmetric structure and near-filed soil regions are represented by the standard finite elements, while the unbounded multi-layered far-field soil medium is modeled by the dynamic infinite elements developed by the present authors (Yun *et al.* 1995). The proposed technique is verified utilizing several cylindrical tanks on a rigid ground and a homogeneous elastic half-space, for which solutions by other researcher are available. Finally, an application example of a reinforced concrete tank on a horizontally layered soil medium with a rigid bedrock is presented to demonstrate the beneficial effect of the soil-structure interaction on the member forces of the liquid storage tank subject to earthquake loading.

2. Equation of motion

Fig. 1 describes an axisymmetirc fluid-structure-soil interaction system investigated in this study, which can be effectively defined in the cylindrical coordinate system (r, θ, z). The Fourier series expansion method in the circumferential direction (θ) is employed to express the geometry and

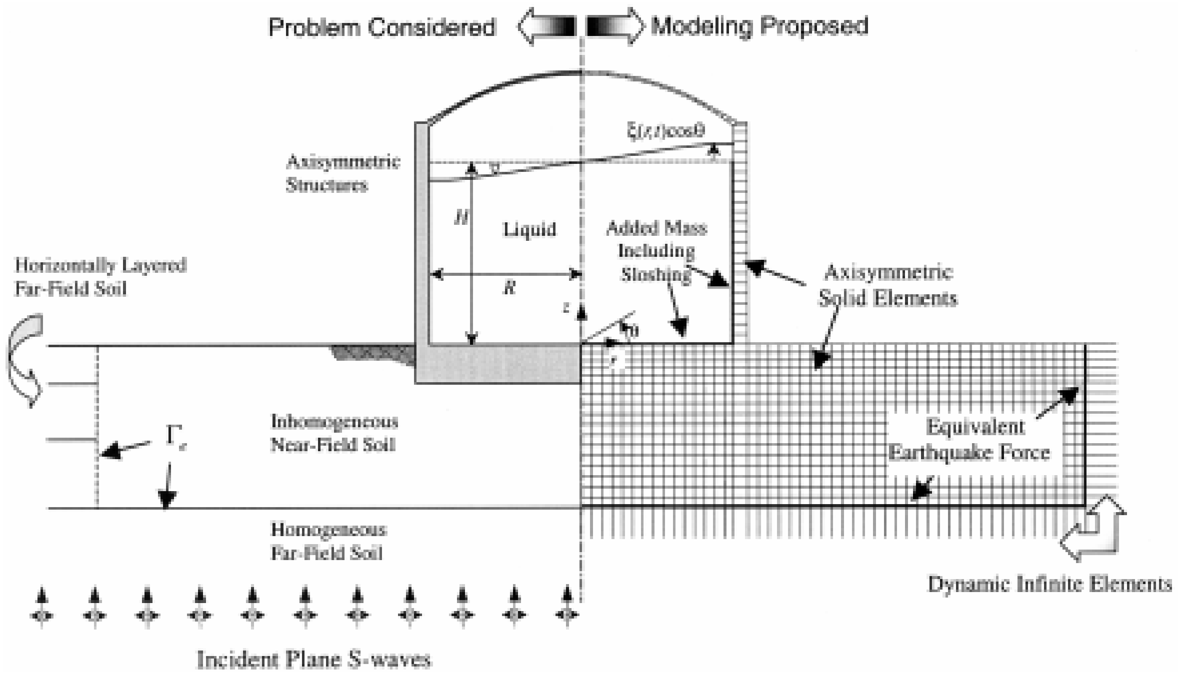

Fig. 1 Fluid-structure-soil interaction problem and its modeling in this study

motions of the system. The seismic input, on the other hand, is assumed as a plane-symmetric vertically incident S-waves, which results in a single equation of motion for the Fourier component of order one.

In this study, the fluid is assumed to be incompressible and inviscid, and its motion is regarded as irrotational. Then, its interaction motion with the encompassing structure is modeled by a generalized frequency-dependent added mass including the sloshing effect of the liquid. Finite elements are used to represent the behaviors of the structure and near-field soil regions, while dynamic infinite elements for the unbounded far-field soil. The equation of motion for the total fluid-structure-soil system subjected to the horizontal seismic input is then constructed in the frequency domain.

2.1 Modeling of contained fluid

2.1.1 Velocity potential function for fluid motion

The displacement field in the cylindrical structure and soils subjected to horizontal earthquake can be written as

$$u(r, \theta, z, t) = U(r, z, t)\cos\theta \tag{1a}$$

$$v(r, \theta, z, t) = -V(r, z, t)\sin\theta \tag{1b}$$

$$w(r, \theta, z, t) = W(r, z, t)\cos\theta \tag{1c}$$

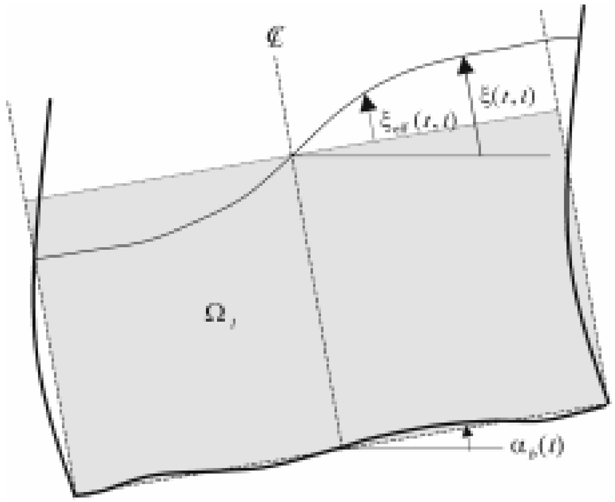

Fig. 2 Definitions of sloshing responses in a plane with $\theta = 0$

where $u(r, \theta, z, t)$, $v(r, \theta, z, t)$, and $w(r, \theta, z, t)$ denote displacement functions in the (r, θ, z) cylindrical coordinates.

Referring to Fig. 2, for the irrotational flow, the velocity potential function, $\phi(r, \theta, z, t)$, and the sloshing height representing the elevation of the free surface over the mean surface level, $\zeta(r, \theta, t)$, in the cylindrical fluid region (Ω_f) can be expressed as

$$\phi(r, \theta, z, t) = \varphi(r, z, t)\cos\theta \tag{2a}$$

$$\zeta(r, \theta, t) = \xi(r, t)\cos\theta \tag{2b}$$

Then, the velocity of a fluid particle in the nth generalized coordinate, v_n, can be obtained as

$$v_n = \frac{\partial\phi}{\partial n} \tag{3}$$

and the corresponding hydrodynamic pressure, $p_d(r, \theta, z, t)$, for the inviscid liquid can be computed as

$$p_d(r, \theta, z, t) = -\rho\frac{\partial\phi}{\partial t} \tag{4}$$

where ρ is the mass density of the liquid.

The velocity potential function must satisfy the Laplace equation to fulfill the continuity condition of the incompressible fluid as

$$\frac{\partial^2\varphi}{\partial r^2} + \frac{1}{r}\frac{\partial\varphi}{\partial r} - \frac{1}{r^2}\varphi + \frac{\partial^2\varphi}{\partial z^2} = 0 \quad \text{in} \quad \Omega_f \tag{5}$$

This equation is supplemented by the boundary conditions on the fluid-structure interface and the free surface of the inviscid fluid for the horizontal earthquake as

$$\frac{\partial \varphi}{\partial r} = \dot{U}_s(z, t) \qquad \text{on wetted shell } (r = R) \tag{6}$$

$$\frac{\partial \varphi}{\partial z} = \dot{W}_b(r, t) \qquad \text{on wetted base } (z = 0) \tag{7}$$

$$\rho\dot{\varphi} + \rho g \xi = 0 \qquad \text{on liquid free surface } (z = H) \tag{8}$$

$$\frac{\partial \varphi}{\partial z} = \dot{\xi} \qquad \text{on liquid free surface } (z = H) \tag{9}$$

where R and H are respectively the radius and the height of the fluid domain; $U_s(z, t)$ is the horizontal displacement on the wetted vertical shell (at $\theta = 0$); $W_b(r, t)$ is the vertical displacement on the wetted base of structure (at $\theta = 0$); and g is the gravitational acceleration.

In order to derive a velocity potential function satisfying the governing equation and all the boundary conditions, we start with a solution that meets the boundary condition on the wetted shell given by Eq. (6) as

$$\varphi(r, z, t) = \psi(r, z, t) + r\dot{U}_s(z, t) \tag{10}$$

in which the second term is a particular solution associated with the boundary condition (6), whereas ψ represents a homogeneous solution which satisfies the zero velocity condition on the boundary. The function ψ, which satisfies the Laplace equation and the homogeneous boundary condition at the wetted shell, can be easily obtained using the standard separation of variable method as

$$\psi(r, z, t) = \sum_{n=1}^{\infty} J_1(\lambda_n r) A_n(z, t) \tag{11}$$

in which $J_1(\cdot)$ denotes the Bessel function of the first kind of order one; $\lambda_n = \varepsilon_n / R$; ε_n's are constants satisfying $J_1'(\varepsilon_n) = 0$; and $A_n(z, t)$ is unknown function. The first three of constants ε_n are 1.8411, 5.3314, and 8.5363.

Substituting Eq. (11) into Eq. (10), and applying the weighted residual method with weighting functions of $\{J_1(\lambda_m r)\}_{m=1}^{\infty}$ on the governing Eq. (5) as

$$\int_0^R \sum_{n=1}^{\infty} J_1(\lambda_n r) J_1(\lambda_m r)\left(\frac{d^2 A_n}{dz^2} - \lambda_n^2 A_n\right) r\,dr = -\int_0^R J_1(\lambda_m r)\frac{d^2 \dot{U}_s}{dz^2} r^2\,dr \tag{12}$$

a series of modal differential equations with respect to $A_n(z, t)$ can be obtained as

$$\frac{d^2 A_n}{dz^2} - \lambda_n^2 A_n = -\beta_n \frac{d^2 \dot{U}_s}{dz^2} \qquad (n = 1, 2, 3, \ldots) \tag{13}$$

where

$$\beta_n = \frac{2R}{(\varepsilon_n^2 - 1) J_1(\varepsilon_n)} \tag{14}$$

In this study, the free surface elevation $\xi(r, t)$ and the vertical displacement on the wetted base $W_b(r, t)$ are expanded using the Bessel functions, and horizontal displacement on the wetted shell $U_s(z, t)$ is represented as the third order polynomials of z as

$$\xi(r, t) = \sum_{m=1}^{n_m} J_1(\lambda_m r)\eta_m(t) \tag{15}$$

$$W_b(r, t) \cong \overline{W}_b(r, t) = \sum_{m=1}^{n_m} J_1(\lambda_m r) q_m(t) \tag{16}$$

$$U_s(z, t) \cong \overline{U}_s(z, t) = \boldsymbol{p}(z)^T \boldsymbol{c}(t) \tag{17}$$

where $\boldsymbol{p}(z) = [1, z, z^2, z^3]^T$; $\boldsymbol{c}(t) = [c_0(t), c_1(t), c_2(t), c_3(t)]^T$; $\eta_m(t)$, $q_m(t)$, and $c_m(t)$ are the generalized coordinates; n_m is the number of Bessel functions used; and the superscript T stands for transpose of a matrix. Accordingly, the boundary conditions (7) and (8) can be rewritten as the modal boundary conditions associated with the function $A_n(z, t)$ in the weighted residual sense as

$$\frac{dA_n}{dz} + \beta_n \left\{ \frac{d\boldsymbol{p}(z)}{dz} \right\}^T \dot{c}(t) = \dot{q}_n \quad \text{at} \quad z = 0 \tag{18a}$$

$$\dot{A}_n + \beta_n \boldsymbol{p}(z)^T \ddot{\boldsymbol{c}}(t) + g\eta_n = 0 \quad \text{at} \quad z = H \tag{18b}$$

Then, the function $A_n(z, t)$ which satisfies the governing Eq. (13) and the boundary conditions (18a) and (18b) can be derived in terms of the generalized coordinates, $\eta_n(t)$, $q_n(t)$, and $c_m(t)$, as

$$\begin{aligned} A_n(z;t) = & -\beta_n \frac{\cosh(\lambda_n z)}{\cosh(\lambda_n H)} \dot{c}_1(t) \\ & -\beta_n \left\{ \frac{\cosh(\lambda_n z)}{\cosh(\lambda_n H)} \left(H - b_n \frac{\sinh(\lambda_n H)}{\lambda_n} \right) + \frac{\sinh(\lambda_n z)}{\lambda_n} \right\} \dot{c}_2(t) \\ & -\beta_n \left\{ \frac{\cosh(\lambda_n z)}{\cosh(\lambda_n H)} \left(H^2 + \frac{2}{\lambda_n^2} \right) - \frac{2}{\lambda_n^2} \right\} \dot{c}_3(t) \\ & -\beta_n \left\{ \frac{\cosh(\lambda_n z)}{\cosh(\lambda_n H)} \left(H^3 + \frac{6H}{\lambda_n^2} - \frac{6}{\lambda_n^3} \sinh(\lambda_n H) \right) + \frac{6}{\lambda_n^3} \sinh(\lambda_n z) - \frac{6}{\lambda_n^2} z \right\} \dot{c}_4(t) \\ & -\frac{1}{\lambda_n} \{ \tanh(\lambda_n H)\cosh(\lambda_n z) - \sinh(\lambda_n z) \} \dot{q}_n(t) \\ & -g \frac{\cosh(\lambda_n z)}{\cosh(\lambda_n H)} \int_0^t \eta_n(\tau) d\tau \end{aligned} \tag{19}$$

In this study, the generalized coordinates, $q_n(t)$ and $c_m(t)$, associated with the structural motion are related to the finite element solutions, $\boldsymbol{d}_s(t)$ and $\boldsymbol{d}_b(t)$, by means of the weighted residual method as

$$\int_0^H \delta U_s(U_s - \overline{U}_s)dz = 0 \quad \text{or} \quad \boldsymbol{c}(t) = \boldsymbol{R}_s \boldsymbol{d}_s(t) \tag{20a}$$

$$\int_0^R \delta W_b(W_b - \overline{W}_b)rdr = 0 \quad \text{or} \quad \boldsymbol{q}(t) = \boldsymbol{R}_b \boldsymbol{d}_b(t) \tag{20b}$$

where δU_s and δW_b denote arbitrary weighting functions; $\boldsymbol{q}(t) = [q_1(t), q_2(t), q_3(t), \ldots]^T$; and $\boldsymbol{R}_s$ and $\boldsymbol{R}_b$ are the constant matrices.

After a lengthy derivation from Eqs. (11), (19) and (20), the velocity potential function $\varphi(r, z, t)$ shown in Eq. (10) can be obtained as

$$\varphi(r, z, t) = \sum_{n=1}^{\infty} \beta_n J_1(\lambda_n r)\{\boldsymbol{E}_n(z)\}^T \boldsymbol{R}_s \dot{\boldsymbol{d}}_s(t) + \{\tilde{\boldsymbol{E}}(z)\}^T \boldsymbol{J}(r) \boldsymbol{R}_b \dot{\boldsymbol{d}}_b(t)$$
$$- g\{\boldsymbol{CH}(z)\}^T \boldsymbol{J}(r) \int_0^t \{\boldsymbol{\eta}(\tau)\} d\tau \tag{21}$$

where

$$\{\boldsymbol{E}_n(z)\} = [E_{n0}(z), E_{n1}(z), E_{n2}(z), E_{n3}(z)]^T \tag{22a}$$

$$\boldsymbol{J}(r) = diag[J_1(\lambda_m r)] \tag{22b}$$

$$[\tilde{\boldsymbol{E}}(z)] = [\tilde{E}_1(z), \tilde{E}_2(z), \tilde{E}_3(z), \ldots]^T \tag{22c}$$

$$\{\boldsymbol{CH}(z)\} = \left[\frac{\cosh(\lambda_1 z)}{\cosh(\lambda_1 H)}, \frac{\cosh(\lambda_2 z)}{\cosh(\lambda_2 H)}, \frac{\cosh(\lambda_3 z)}{\cosh(\lambda_3 H)}, \ldots\right]^T \tag{22d}$$

$$\{\boldsymbol{\eta}(t)\} = [\eta_1(t), \eta_2(t), \eta_3(t), \ldots]^T \tag{22e}$$

in which $diag[a_m]$ is defined as a diagonal matrix with its mth diagonal component of a_m; and $E_{nm}(z)$ and $\tilde{E}_n(z)$ are analytical functions given in Appendix A1. The first two terms in Eq. (21) represent the impulsive components which account for the fluid motion interacting with the structural motion, while the last term is the convective contribution by the sloshing response of the liquid. The unknown function $\{\eta(t)\}$ related to the sloshing response in Eq. (21) can be represented in terms of accelerations of the structure on the wetted boundaries, which will be described in the next section.

2.1.2 Sloshing response

The sloshing response of the liquid can be expressed as an uncoupled equation of motion for the generalized coordinate $\{\eta(t)\}$ by substituting Eqs. (21) and (15) into the kinematic relation at the free surface as in Eq. (9) as

$$\boldsymbol{M}_{\eta\eta}\{\ddot{\eta}(t)\} + \boldsymbol{C}_{\eta\eta}\{\dot{\eta}(t)\} + \boldsymbol{K}_{\eta\eta}\{\eta(t)\} = \boldsymbol{Q}_{\eta s}\ddot{\boldsymbol{d}}_s(t) + \boldsymbol{Q}_{\eta b}\ddot{\boldsymbol{d}}_b(t) \tag{23}$$

where $\boldsymbol{M}_{\eta\eta}$, $\boldsymbol{C}_{\eta\eta}$, and $\boldsymbol{K}_{\eta\eta}$ are diagonal matrices; $\boldsymbol{Q}_{\eta s}$ and $\boldsymbol{Q}_{\eta b}$ are participation coefficient matrices; and $\ddot{\boldsymbol{d}}_s(t)$ and $\ddot{\boldsymbol{d}}_b(t)$ are the acceleration vectors of the structure on the wetted shell and bottom. The coefficient matrices are described in Appendix A2. In the sloshing equation, the viscosity of the fluid is included in the damping matrix. Once the structural responses are calculated, the sloshing responses can be easily obtained using a standard direct integration scheme such as the Newmark-β method in the time domain.

It is to note that undamped sloshing frequency ω_{sn}, which can be obtained from Eq. (23), is the same as the one for a rigid cylindrical tank fixed on the rigid ground as (Haroun 1983)

$$\omega_{sn} = \sqrt{g\frac{\varepsilon_n}{R}\tanh\left(\varepsilon_n\frac{H}{R}\right)} \tag{24}$$

In a design stage, sufficient freeboard shall be provided to prevent the overflow of the contained liquid and the large impact force on the roof structure. To determine the required freeboard, the sloshing response $\xi(r, t)$ has to be corrected to obtain the effective sloshing height $\xi_{eff}(r, t)$ defined in Fig. 2 as

$$\xi_{eff}(r,t) = \xi(r,t) - r\alpha_b(t) \tag{25}$$

where $\alpha_b(t)$ is average rotation of the base.

2.1.3 Generalized added mass associated with fluid motion

The equivalent nodal force vectors, $\boldsymbol{f}_s(t)$ and $\boldsymbol{f}_b(t)$, associated with the hydrodynamic pressure on the wetted boundaries are obtained using the potential solution derived in Eq. (21) and the principle of virtual work as

$$\boldsymbol{f}_s(t) = -\rho\pi R\int_0^H\{\boldsymbol{N}_{\overline{U}_s}(z)\}\dot{\varphi}(R,z,t)dz \tag{26a}$$

$$\boldsymbol{f}_b(t) = -\rho\pi\int_0^R\{\boldsymbol{N}_{\overline{W}_b}(r)\}\dot{\varphi}(r,0,t)rdr \tag{26b}$$

which results in

$$\boldsymbol{f}_s(t) = -\hat{\boldsymbol{M}}_{ss}\ddot{\boldsymbol{d}}_s(t) - \hat{\boldsymbol{M}}_{sb}\ddot{\boldsymbol{d}}_b(t) - \boldsymbol{Q}_{\eta s}^T\{\eta(t)\} \tag{27a}$$

$$\boldsymbol{f}_b(t) = -\hat{\boldsymbol{M}}_{sb}^T\ddot{\boldsymbol{d}}_s(t) - \hat{\boldsymbol{M}}_{bb}\ddot{\boldsymbol{d}}_b(t) - \boldsymbol{Q}_{\eta b}^T\{\eta(t)\} \tag{27b}$$

where $\{\boldsymbol{N}_{\overline{U}_s}(z)\}$ and $\{\boldsymbol{N}_{\overline{W}_b}(r)\}$ are the shape function vectors relating the approximated displacements on the wetted boundaries, $\overline{U}_s$ and $\overline{W}_b$, to their finite element solutions, $\boldsymbol{d}_s(t)$ and $\boldsymbol{d}_b(t)$, as shown in Appendix A3; and $\hat{\boldsymbol{M}}$ denotes the generalized added mass matrix related to the impulsive component of fluid motion as in Appendix A3. Taking Fourier transform of Eq. (27) and obtaining the frequency response of the sloshing motion from Eq. (23), the hydrodynamic force vectors can be expressed in single augmented matrix form in the frequency domain as

$$\boldsymbol{f}_w(\omega) = \hat{\boldsymbol{S}}_{ww}(\omega)\boldsymbol{d}_w(\omega) \tag{28}$$

where

$$\hat{\boldsymbol{S}}_{ww}(\omega) = -\omega^2(\hat{\boldsymbol{M}}_{ww} + \boldsymbol{Q}^T_{\eta w}[\boldsymbol{K}_{\eta\eta} + i\omega\boldsymbol{C}_{\eta\eta} - \omega^2\boldsymbol{M}_{\eta\eta}]^{-1}\boldsymbol{Q}_{\eta w}) \tag{29}$$

in which ω is circular frequency; $\boldsymbol{f}_w = [\boldsymbol{f}_s^T \ \ \boldsymbol{f}_b^T]^T; \boldsymbol{d}_w = [\boldsymbol{d}_s^T \ \ \boldsymbol{d}_b^T]^T$ is the vector of displacement normal to the wetted boundaries; $i = \sqrt{-1}$; the first term $(\hat{\boldsymbol{M}}_{ww})$ on the right hand side of Eq. (29) is the mass associated with the impulsive force of the contained fluid; and the second term $(\boldsymbol{Q}^T_{\eta w}[\boldsymbol{K}_{\eta\eta} + i\omega\boldsymbol{C}_{\eta\eta} - \omega^2\boldsymbol{M}_{\eta\eta}]^{-1}\boldsymbol{Q}_{\eta w})$ is the frequency-dependent added mass matrix related to the convective sloshing motion.

2.2 Modeling of unbounded far-field soil

Referring Fig. 1, the dynamic stiffness matrix of the far-field $\tilde{\boldsymbol{S}}(\omega)$ can be constructed by assembling the element matrices of the infinite elements as (Yang and Yun 1992, Yun *et al.* 1995)

$$\tilde{\boldsymbol{S}}^{(e)}(\omega) = (1 + i2h^{(e)})\tilde{\boldsymbol{K}}^{(e)}(\omega) - \omega^2\tilde{\boldsymbol{M}}^{(e)}(\omega) \tag{30}$$

where $h^{(e)}$ is the hysteretic damping ratio of infinite element (e); and $\tilde{\boldsymbol{K}}^{(e)}(\omega)$ and $\tilde{\boldsymbol{M}}^{(e)}(\omega)$ represent the element stiffness and mass matrices as

$$\tilde{\boldsymbol{K}}^{(e)}(\omega) = \pi \int_{\Omega^{(e)}} \tilde{\boldsymbol{B}}^{(e)}(r, z, \omega)^T \boldsymbol{D}^{(e)} \tilde{\boldsymbol{B}}^{(e)}(r, z, \omega) r dr dz \tag{31}$$

$$\tilde{\boldsymbol{M}}^{(e)}(\omega) = \pi \int_{\Omega^{(e)}} \tilde{\boldsymbol{N}}^{(e)}(r, z, \omega)^T \rho^{(e)} \tilde{\boldsymbol{N}}^{(e)}(r, z, \omega) r dr dz \tag{32}$$

in which $\boldsymbol{D}^{(e)}$ and $\rho^{(e)}$ are the elasticity matrix and the mass density; $\tilde{\boldsymbol{N}}^{(e)}(r, z, \omega)$ is the frequency-dependent shape function matrix for the displacement field; and $\tilde{\boldsymbol{B}}^{(e)}(r, z, \omega)$ denotes the strain matrix associated with $\tilde{\boldsymbol{N}}^{(e)}(r, z, \omega)$. The shape functions of the exponentially decaying types are derived from the approximate wave functions propagating into the infinite direction. Three different types of dynamic infinite elements are constructed. They are the horizontal, vertical, and corner axisymmetric infinite elements. The horizontal and vertical infinite elements have 3 nodes on the interface with the FE region, and the corner element has 1 node as shown in Appendix A4. The shape functions consist of trigonometric functions in the circumferential direction (θ), Lagrange polynomials in the finite direction on the *r-z* plane, and multiple wave functions corresponding to the outgoing primary, shear, and Rayleigh waves in the infinite directions in the *r-z* plane. Thus, they satisfy the compatibility condition along the interface with the FE region and the Sommerfeld radiation condition at infinity (Yun *et al.* 1995). Example shape functions for three types of the infinite elements are shown in Appendix A4.

2.3 Equation of motion for fluid-structure-soil system subjected to earthquake loading

The equation of motion for a fully coupled fluid-structure-soil system subjected to horizontal ground motion can be constructed in frequency domain using the dynamic stiffness matrix of the finite elements for the structure and the near-field soil $\boldsymbol{S}(\omega)$, the impedance matrix of the far-field soil $\tilde{\boldsymbol{S}}_{ee}(\omega)$ on the interface between the near and far-fields (Γ_e), the equivalent earthquake force $\boldsymbol{a}_e^{eqk}(\omega)u_c^{(f)}(\omega)$ applied on Γ_e, and the frequency-dependent added mass matrix of the contained fluid $\hat{\boldsymbol{S}}(\omega)$ shown in Eq. (29) (Yun and Kim 1996) as

$$\begin{bmatrix} \boldsymbol{S}_{ww}(\omega)+\hat{\boldsymbol{S}}_{ww}(\omega) & \boldsymbol{S}_{wn}(\omega) & \boldsymbol{0} \\ \boldsymbol{S}_{nw}(\omega) & \boldsymbol{S}_{nn}(\omega) & \boldsymbol{S}_{ne}(\omega) \\ \boldsymbol{0} & \boldsymbol{S}_{en}(\omega) & \boldsymbol{S}_{ee}(\omega)+\tilde{\boldsymbol{S}}_{ee}(\omega) \end{bmatrix} \begin{Bmatrix} \boldsymbol{d}_w(\omega) \\ \boldsymbol{d}_n(\omega) \\ \boldsymbol{d}_e(\omega) \end{Bmatrix} = \begin{Bmatrix} \boldsymbol{0} \\ \boldsymbol{0} \\ \boldsymbol{a}_e^{eqk}(\omega) \end{Bmatrix} u_c^{(f)}(\omega) \tag{33}$$

where the subscript w denotes the degrees of freedom normal to the fluid region along the wetted boundary between the structure and fluid; the subscript e represents those on the interface between the finite elements and the infinite elements (Γ_e); n is those in near field except w and e; $u_c^{(f)}(\omega)$ is the earthquake input as a control motion in the free field analysis; and $\boldsymbol{a}_e^{eqk}(\omega)$ is the effective earthquake-load coefficient vector. In this study, $\boldsymbol{S}(\omega)$ for the structure and the near-field soil is computed using the axisymmetric solid elements with 9-nodes, and $\tilde{\boldsymbol{S}}_{ee}(\omega)$ for the far-field soil is calculated using the dynamic infinite elements and the static condensation technique.

The effective earthquake-load coefficient vector $\boldsymbol{a}_e^{eqk}(\omega)$ can be obtained using $\tilde{\boldsymbol{S}}_{ee}(\omega)$ and the free field analysis results for the far-field soil layers (Zhao and Valliappan 1992, Kim 1995) as

$$\boldsymbol{a}_e^{eqk}(\omega) = \tilde{\boldsymbol{S}}_{ee}(\omega)\boldsymbol{d}_e^{(f)}(\omega) - \boldsymbol{A}\boldsymbol{t}_e^{(f)}(\omega) \tag{34}$$

where $\boldsymbol{d}_e^{(f)}(\omega)$ and $\boldsymbol{t}_e^{(f)}(\omega)$ are the free field displacement and the traction vectors on Γ_e due to a unit harmonic control motion with ω; and $\boldsymbol{A}$ is a constant matrix transforming the traction on Γ_e to the nodal force vector.

The responses of the structure and near-field soil region can be obtained by solving Eq. (33) in frequency domain. In general, the frequency response function matrix, which is the inverse of the first term on the left hand side of Eq. (33), is evaluated at a limited number of frequency points, then the results are interpolated to other frequency points for computational efficiency (Clough and Penzien 1993). Then the time history responses are evaluated by the inverse Fourier transform of the responses in frequency domain. The sloshing response is computed using Eq. (23) in time domain by the Newmark-β method.

3. Numerical examples

3.1 Verification examples

For verification of the present method, a couple of example analyses are performed. The first one is an earthquake response analysis for tall and broad cylindrical tanks on rigid ground. The second one is a free vibration analysis of a cylindrical tank on a compliant homogeneous half-space. The

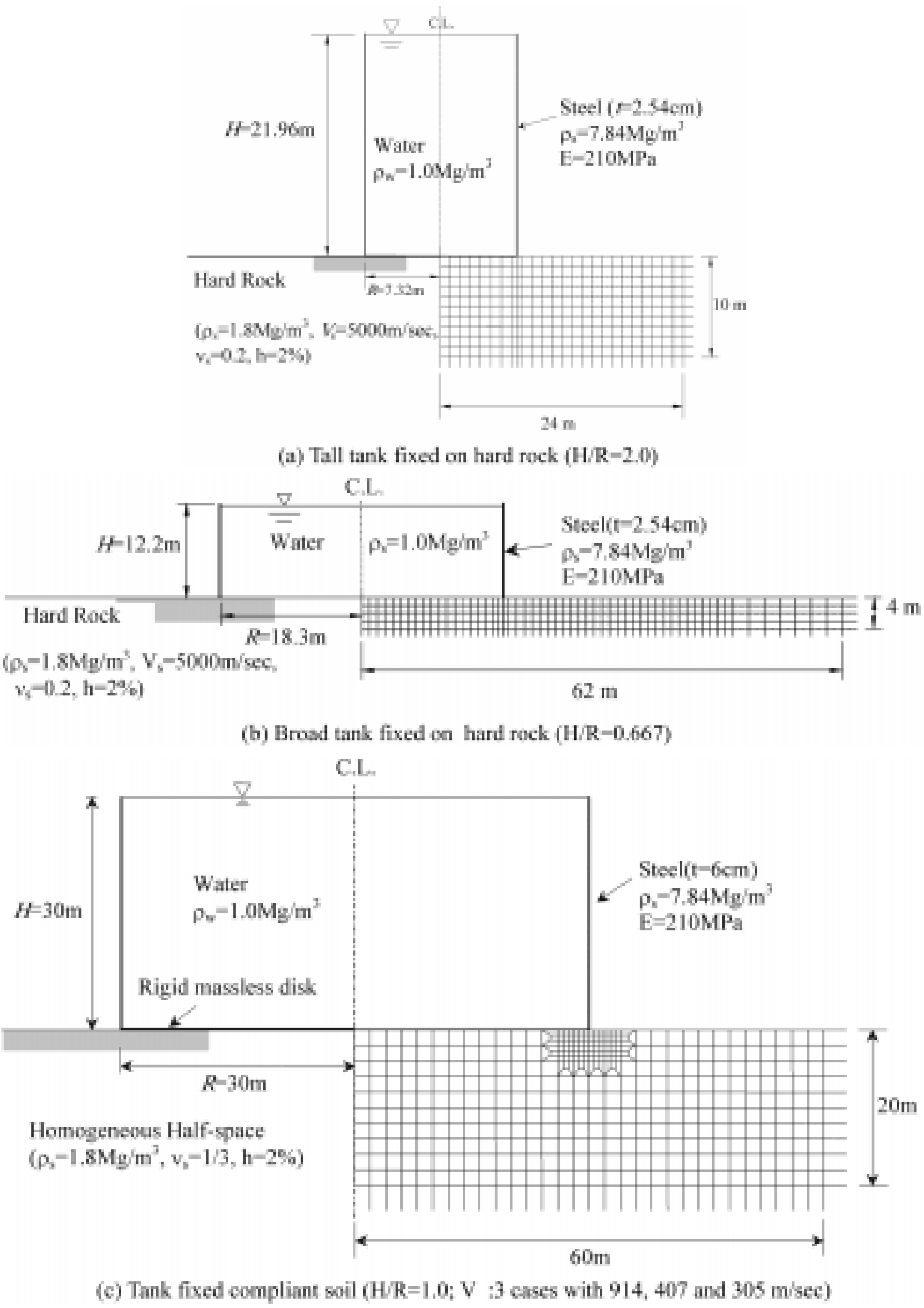

Fig. 3 Verification examples

results are respectively compared with the solutions by Haroun (1983) and Veletsos and Tang (1990).

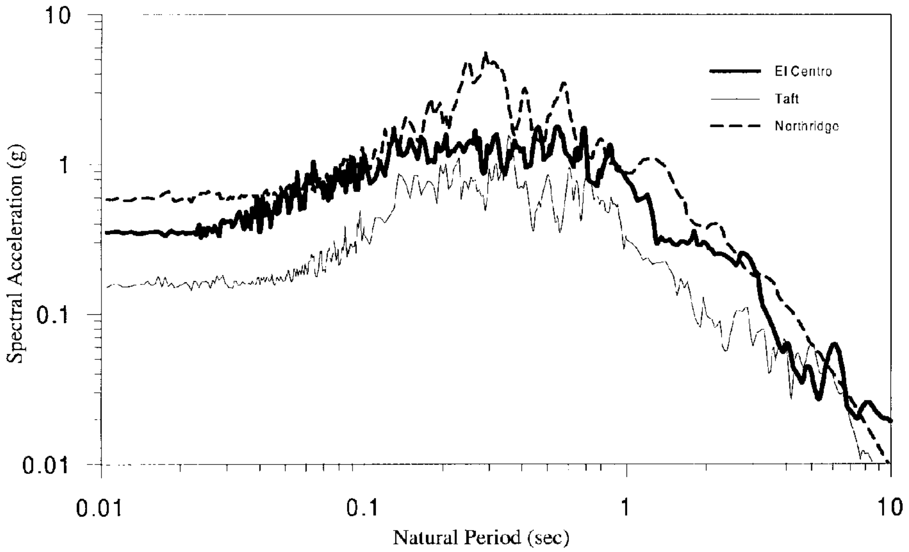

Fig. 4 Acceleration response spectra of input ground motions (0.5% damping)

Table 1 Maximum responses of broad and tall tanks for El Centro earthquake

	Tall tank				Broad tank			
	Housner (1963)	Haroun (1983)	Present study*	Diff.** (%)	Housner (1963)	Haroun (1983)	Present study*	Diff.** (%)
Natural frequency (Hz)	N/A	5.29	5.43	2.6	N/A	6.17	6.37	3.2
Base shear (MN)	11.0	23.0	21.9 (21.6)	4.8 (6.1)	18.1	39.7	37.2 (24.1)	6.3 (39.3)
Base moment (MN-m)	107	278	243 (233)	12.6 (16.2)	88.5	200	183 (123)	8.5 (38.5)

Notes: *Results using ten Bessel functions; and those in parentheses are using one Bessel function.
**Difference between the present and the Haroun's results.

3.1.1 Flexible steel tanks fixed on rigid ground

Earthquake response analyses are carried out for two typical types of liquid storage tanks (i.e., broad and tall cylindrical tanks) fixed on rigid ground. The geometrical configuration, the mechanical properties of the tanks, and their discretized meshes for the tanks and soil medium are depicted in Figs. 3a and 3b. The vertical wall is modeled by 22 axisymmetric solid elements with 9 nodes for tall tank and 13 elements for broad tank. The rigid ground is modeled as a hard rock medium with the shear wave velocity (V_s) of 5000 m/s in the present analysis. The soil region is modeled by axisymmetric solid elements with 9 nodes and axisymmetric infinte elements with 3 nodes. El Centro acceleration record (NS-component, peak ground acceleration (PGA) = 0.348 g, 1940) is utilized as the input ground motion. The accelerations recorded during Taft (N21E, PGA = 0.156 g, 1952) and Northridge (Newhall, EW-component, PGA = 0.583 g, 1994) earthquakes are

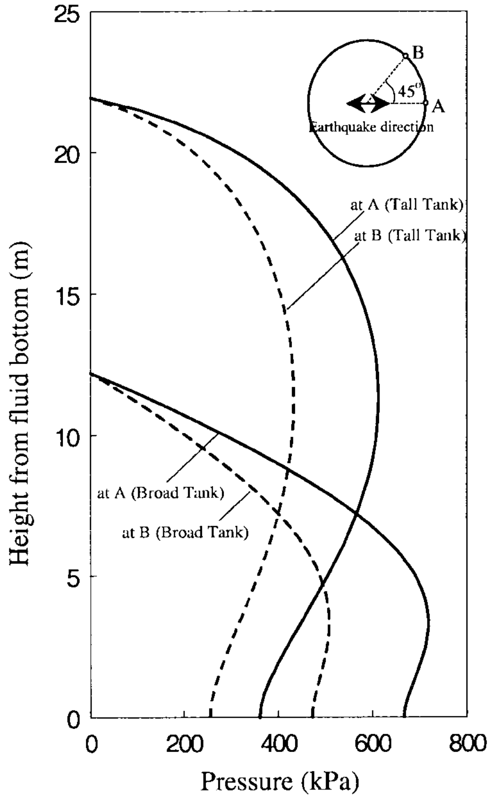

Fig. 5 Hydrodynamic pressure profiles at the time instants for maximum base shear (El Centro NS-component, 1940)

Table 2 Maximum sloshing heights for various earthquakes (unit : cm)

Input earthquake	Tall tank		Broad tank	
	Haroun	Present study*	Haroun	Present study*
El Centro	37.9	51.9 (38.2)	35.2	44.1 (35.6)
Taft	38.3	39.2 (38.4)	42.6	44.8 (41.9)
Northridge	68.7	83.2 (69.8)	43.3	63.5 (43.6)

Notes: *Results using twenty sloshing modes; and those in parentheses are using one sloshing mode.

also considered to calculate the maximum sloshing height. Damping ratio is assumed to be 2.0% for the steel structure and 0.5% for the sloshing motion. Acceleration response spectra (0.5% damping ratio) for those earthquakes are shown in Fig. 4.

The maximum earthquake responses are summarized in Table 1 along with those by Housner (1963) and Haroun (1983). The Housner's solutions were computed for rigid tanks, while the Haroun's solutions were based on a simplified model for the contained fluid and the flexible tank

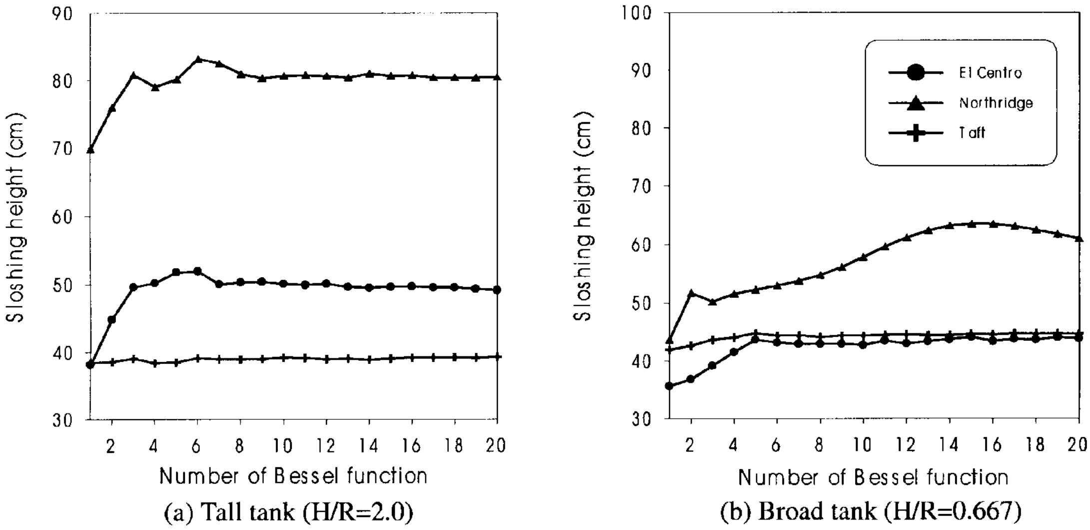

Fig. 6 Maximum sloshing height depending on number of Bessel functions included in analysis

and using the response spectrum method. The maximum base shear and moment on the flexible tanks by the present method are found to be reasonably close to those by the Haroun's mothod: the maximum difference between two sets of results are about 12.6%. However, they are significantly larger than those for the rigid tanks, owing to the impulsive fluid motion component associated with $\hat{\boldsymbol{M}}_{ww}$ in Eq. (29) amplified by the flexibility of the shell. The hydrodynamic pressure profiles for two tanks are shown in Fig. 5. The location of the maximum pressure moves upward in the tall tank in comparison with the broad tank, which implies that the effects of the shell flexibility are more substantial in the tall tank. These results are consistent with those by other researchers, e.g., Haroun (1983). The effects of the number of Bessel functions used in the analysis are investigated for two cases with one and ten components. The results in Table 1 indicate that one Bessel function may be used to obtain reasonable member forces for tall tanks, where as more components, for instance 10, shall be used for broad tanks.

Sloshing heights are calculated for the three earthquake inputs to investigate the effects of the number of the sloshing modes(i.e., Bessel functions) included in the analysis. Two cases using one and twenty sloshing modes are compared along with those by Haroun's method. The maximum sloshing heights are listed in Table 2. In the Haroun's method, the sloshing height is computed utilizing one sloshing mode and the response spectrum method. As in Table 2, the sloshing heights by the present method with one mode are in good agreements with those by Haroun's method. However, the sloshing heights using twenty sloshing modes are considerably larger than those using one mode. The maximum sloshing heights are plotted against the number of Bessel functions included in Fig. 6. The maximum sloshing height generally remains constant, if the first six sloshing modes are included in the analysis. However, for the case of broad tank subjected to Northridge earthquake, the effect of higher (6^{th} to 20^{th}) modes is found to be still significant as in Fig. 6. It is due to the high spectral acceleration of Northridge earthquake in the range of 1 to 2 sec. (Fig. 4), which corresponds to the sloshing periods of those higher modes. The results suggest that a

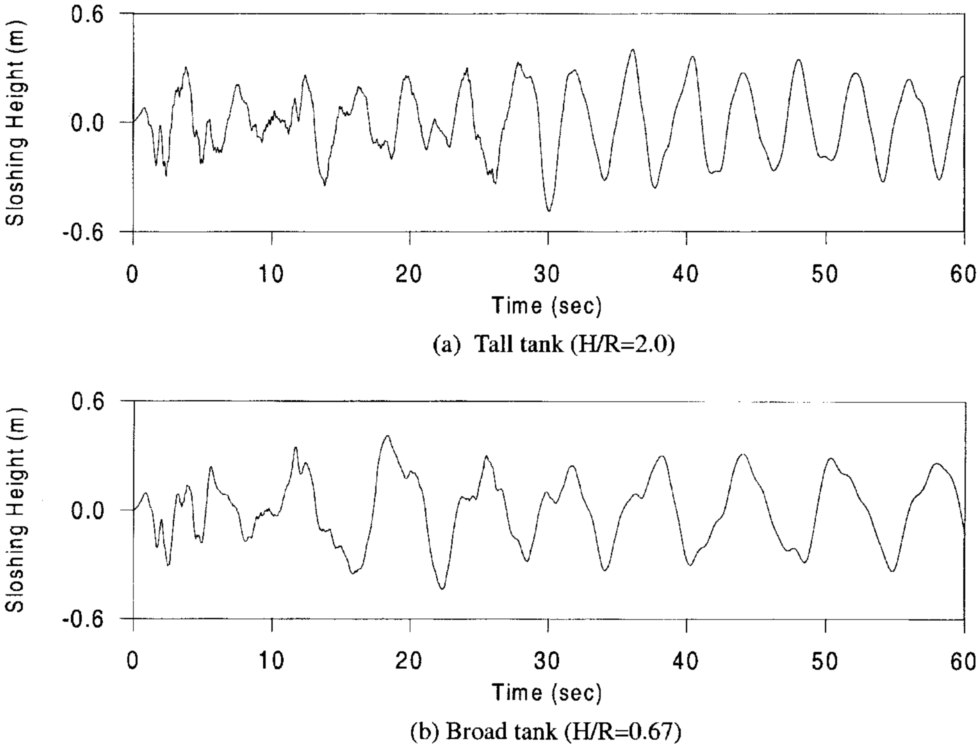

Fig. 7 Time histories of sloshing responses using 20 sloshing modes (El Centro NS-component, 1940)

Table 3 Fundamental natural frequency ratios of steel tanks for various H/R ratios and V_s

V_s (m/sec)	Filling ratios (H/R)			
	0.5	1.0	2.0	3.0
914 (3000 ft/sec)	0.947 (0.952)	0.939 (0.931)	0.930 (0.931)	0.940 (0.930)
457 (1500 ft/sec)	0.863 (0.865)	0.785 (0.788)	0.782 (0.782)	0.796 (0.791)
305 (1000 ft/sec)	0.812 (0.800)	0.624 (0.643)	0.641 (0.638)	0.662 (0.646)

Notes: 1. The natural frequency ratio is defined as the ratio to the natural frequency for a rigid round case.
2. Values in parentheses are from Veletsos and Tang (1990).

sufficient number of the sloshing modes have to be used in the sloshing analysis taking into account the size of the tank and the frequency contents of the input earthquake motion. Similar results were reported for a broad rectangular liquid storage tank subjected to an earthquake with large long period components such as Mexico City earthquake by Choun and Yun (1999).

Time histories of the sloshing heights for El Centro earthquake are shown in Fig. 7. It can be observed that the sloshing motions last much longer than the duration of the earthquake excitation, and there is a large difference between the time instances for the maximum sloshing height and the peak ground acceleration. These are due to the long sloshing periods and the small liquid damping.

3.1.2 Flexible steel tank on compliant homogeneous half-space

The effectiveness of the present method is investigated for fluid-structure-soil interaction analysis using a cylindrical tank on a compliant homogeneous half-space shown in Fig. 3c. The first natural frequencies are computed for various height/radius (H/R) and shear wave velocities of the soil, then those values are normalized to the natural frequency for a hard rock condition ($V_s = 5000$ m/sec). The frequency ratios are compared with those by Veletsos and Tang (1990) in Table 3. Two sets of the results are in good agreements, which indicates the validity of the present formulation for the fluid-structure-soil interaction analysis. The results in Table 3 show that the natural frequency decreases significantly as the stiffness of the soil decreases, and such a trend becomes more

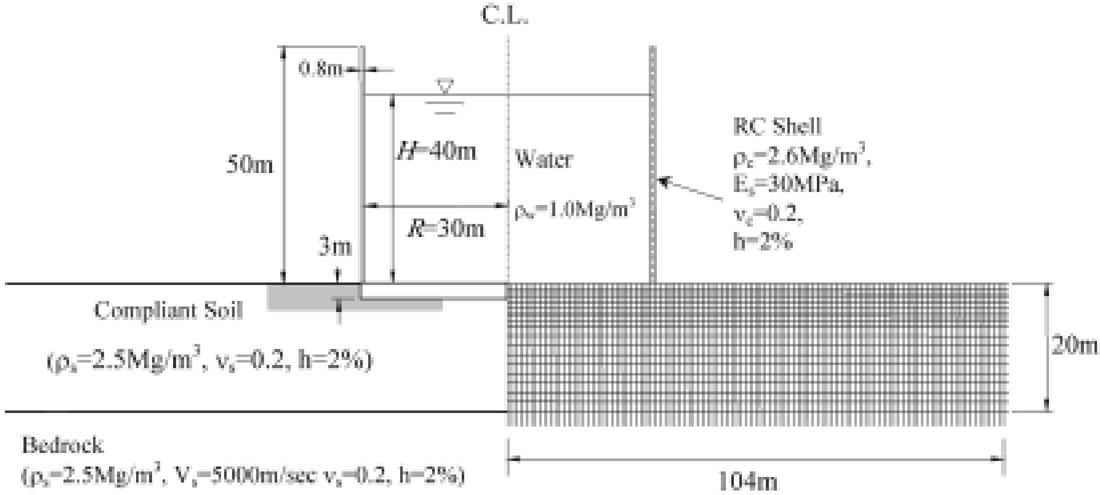

Fig. 8 RC liquid storage tank and its meshes of finite and infinite elements
(V_s of compliant soil : 3 cases with 500, 800, and 5000 m/sec.)

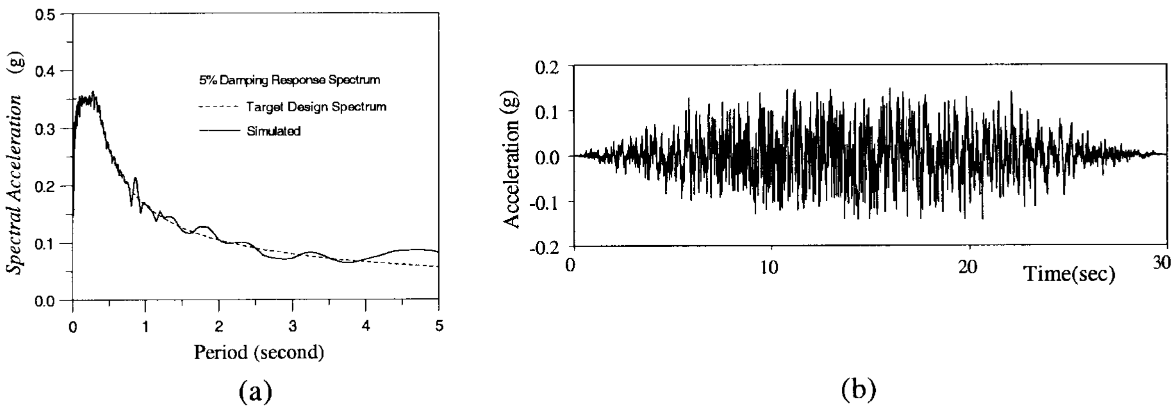

Fig. 9 Simulated control acceleration used as outcrop motion at the top of bedrock (PGA = 0.14 g)

apparent for the case of a high *H/R* ratio. These results indicate that accurate dynamic analysis considering the fluid-structure-soil interaction is required to achieve safe and economical designs especially for tall tanks on soft ground condition.

3.2 Application example flexible RC tank on a layered half-space

In order to gain insight of the soil-structure interaction effect on the member forces of a liquid storage tank, a stress analysis is carried out for a structure depicted in Fig. 8 under various soil

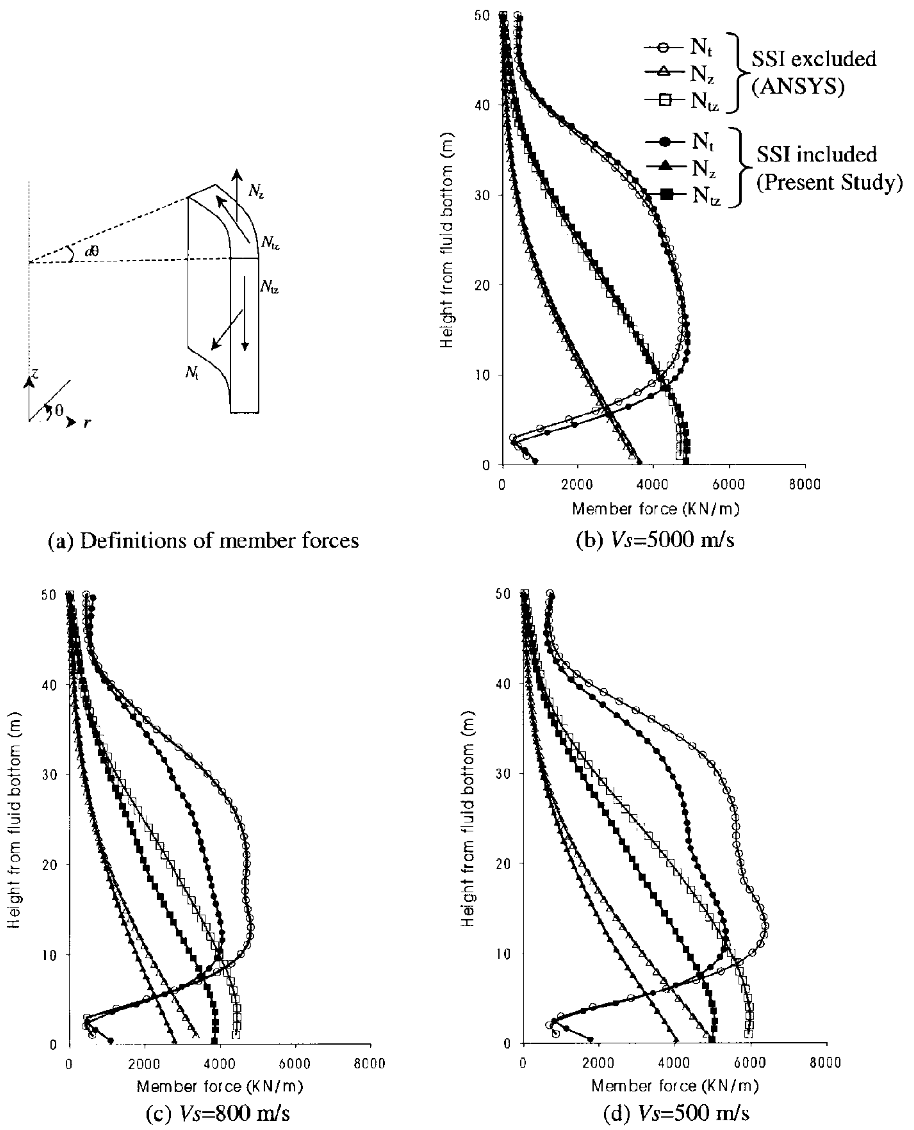

Fig. 10 Maximum member force profiles for a RC liquid storage tank (N_t at $\theta = 0^{\circ}$, N_z at $\theta = 0^{\circ}$, and N_{tz} at $\theta = 90^{\circ}$)

conditions. The structure is supported by a horizontal layer with the underlying bedrock. Three values of the shear wave velocity for the horizontal soil layer, i.e., 500 m/s, 800 m/s, and 5000 m/s, are considered in this investigation. The other material properties for the structure and soil regions are given in Fig. 8. Ten components of Bessel functions are included in this analysis to describe the fluid motion. An acceleration time history with PGA of 0.14 g, which is compatible with a design response spectrum for a rock site given in Fig. 9a, is simulated for the earthquake input as in Fig. 9b. In this analysis, the control acceleration is assigned at the top of bedrock as a horizontal outcrop motion. Thus, seismic motion can be amplified at the ground surface depending on the properties of the horizontal soil layer.

Member forces are calculated on the vertical shell for three different soil conditions including both the fluid-structure interaction and soil-structure interaction by present method, and their maximum values are plotted along the height of the structure in Fig. 10. For the purpose of comparison, the maximum member forces are also computed using ANSYS program (1999) for the same structure but on a rigid ground. A fully coupled fluid-structure-soil interaction analysis cannot be carried out by ANSYS program. In ANSYS analysis, the input ground acceleration at the fixed base is prepared for each soil condition by carrying out the free-field analysis using SHAKE91 program (Schnabel *et al*. 1991). Thus, the solution by ANSYS can be considered as the response for the same input motion but excluding the soil-structure interaction effect. Two sets of the results for a rigid soil condition by the present and ANSYS analysis (in Fig. 10b) are found in good agreements, which confirms the accuracy of the present analysis. The results for the softer soil conditions in Figs. 10c and 10d indicate that the member forces on the shell reduce considerably as the soil stiffness decreases. This result re-confirms that accurate dynamic analysis of a large liquid storage tank considering the soil-structure interaction may yield cost-effective cross-section for the structure.

4. Conclusions

This paper presented a fully coupled fluid-structure-soil interaction analysis technique for cylindrical liquid-contained structures subjected to a horizontal ground excitation. A new closed-form velocity potential solution was derived for the motion of the liquid considering the effects of the horizontal and rocking motions of the structure, the structural flexibility, and the liquid sloshing. The structure and the near-field soil region were modeled by the axisymmetric finite elements, while the far-field soil regions were modeled by the axisymmetric dynamic infinite elements. Finally the equation of motion for the fully coupled fluid-structure-soil system is obtained in the frequency domain considering the fluid-structure interaction represented by a frequency dependent added mass matrix.

The present method was first verified for tall and broad tanks on rigid foundation. Then accuracy of modeling the fluid-structure-soil interaction is confirmed by comparing the natural frequencies for various cases of cylindrical tanks on a homogeneous half-space with the reference solutions. Those comparisons show that the proposed method can be effectively used for the seismic analysis of the cylindrical liquid storage structures with compliant ground condition. In addition, the results of a seismic response analysis for a liquid storage tank on a horizontal layer with rigid bedrock indicate that accurate dynamic analysis of a large liquid storage tank including the soil-structure interaction effects can yield cost-effective cross-section for the structure.

Acknowledgements

This work was supported by the interdisciplinary research program of the Korea Science and Engineering Foundation (Grant No. 1999-1-311-001-3), and partially by Samsung Corporation.

References

ANSYS Inc. (1999), ANSYS 5.5, User's Reference Manual.

Balendra, T., Ang, K.K., Paramasivam, P. and Lee, S.L. (1982), "Seismic design of flexible cylindrical liquid storage tanks", *Earthq. Eng. & Struct. Dyn.*, **10**, 477-498.

Choun, Y.-S. and Yun, C.-B. (1999), "Sloshing analysis of rectangular tanks with a submerged structure by using small-amplitude water wave theory", *Earthq. Eng. & Struct. Dyn.*, **28**, 763-783.

Clough, R.W. and Penzien, J. (1993), *Dynamics of Structures*, 2nd edn., McGraw-Hill.

Haroun, M.A. (1983), "Vibration studies and tests of liquid storage tanks", *Earthq. Eng. & Struct. Dyn.*, **11**, 179-206.

Haroun, M.A. and Abou-Izzeddine, W. (1992), "Parametric study of seismic soil-tank interaction. I: horizontal excitation", *J. Struct. Eng.*, ASCE, **118**(3), 783-812.

Hori, N. (1990), "Effects of soil on the dynamic response of liquid-tank system", *Pressure Vessel and Piping Division*, ASME, **112**, 118-123.

Housner, G. (1963), "The dynamic behavior of water tank", *Bulletin of the Seismological Society of America*, **53**, 381-387.

Kim, J.-M. (1995), "Development of axisymmetric dynamic infinite element based on multiple wave functions and its application to soil-structure interaction analysis", *Ph.D. Thesis*, Dept. of Civil Eng., Korea Advanced Institute of Science & Technology.

Natsiavas, S. (1990), "Simplified models for dynamic response of tall unanchored liquid containers", *Pressure Vessel and Piping Division*, ASME, **112**, 124-131.

Seebar, R., Fischer, F.D. and Rammerstorfer (1990), "Analysis of a three-dimensional tank-liquid-soil interaction problem", *Pressure Vessel and Piping Division*, ASME, **112**, 28-33.

Schnabel, P.B., Lysmer, J. and Seed, H.B. (1991), "SHAKE91, A computer program for earthquake response analysis of horizontally layered sites", EERC(Earthquake Engineering Research Center), College of Engineering, University of California Berkeley, California.

Veletsos, A.S. and Tang, Y. (1990), "Soil-structure interaction effects for laterally excited liquid storage tanks", *Earthq. Eng. & Struct. Dyn.*, **19**, 473-496.

Wunderlich, W., Schapertons, B. and Temme, C. (1994), "Dynamic stability of non-linear shells of revolution under consideration of the fluid-soil-structure interaction", *Int. J. Numer. Meth. Eng.*, **37**, 2679-2697.

Yang, S.-C. and Yun, C.-B. (1992), "Axisymmetric infinite element for soil-structure interaction analysis", *Eng. Struct.*, **14**, 361-370.

Yun, C.-B. and Kim, J.-M. (1996), "KIESSI-AX3D : A computer program for soil-structure interaction analysis using finite and infinite element techniques", *Research Rep.*, Dept. of Civil Eng., Korea Advanced Institute of Science & Technology.

Yun, C-B., Kim, J-M. and Hyun, C-H. (1995), "Axisymmetric elastodynamic infinite elements for multi-layered half-space", *Int. J. Numer. Meth. Eng.*, **38**, 3723-3743.

Zhao, C. and Valliappan, S. (1993), "An efficient wave input procedures for infinite media", *Commun. Numer. Meth. Numer. Eng.*, **9**, 407-415.

Appendix: Analytical expressions of functions and matrices

(A1) $E_{nm}(z)$ and $\tilde{E}_n(z)$ in Eq. (22) :

$$E_{n0}(z) = 1 - \frac{\cosh(\lambda_n z)}{\cosh(\lambda_n H)}$$

$$E_{n1}(z) = z - \frac{\sinh(\lambda_n z)}{\lambda_n} - \left(H - \frac{\sinh(\lambda_n H)}{\lambda_n}\right)\frac{\cosh(\lambda_n z)}{\cosh(\lambda_n H)}$$

$$E_{n2}(z) = z^2 + \frac{2}{\lambda_n^2} - \left(H^2 + \frac{2}{\lambda_n^2}\right)\frac{\cosh(\lambda_n z)}{\cosh(\lambda_n H)}$$

$$E_{n3}(z) = z^3 + \frac{6}{\lambda_n^2}z - \frac{6}{\lambda_n^3}\sinh(\lambda_n z) - \left(H^3 + \frac{6H}{\lambda_n^2} - \frac{6}{\lambda_n^3}\sinh(\lambda_n H)\right)\frac{\cosh(\lambda_n z)}{\cosh(\lambda_n H)}$$

$$\tilde{E}_n(z) = \frac{1}{\lambda_n}\{\sinh(\lambda_n z) - \tanh(\lambda_n H)\cosh(\lambda_n z)\}$$

(A2) Coefficient matrices in Eq. (23) :

$$\boldsymbol{M}_{\eta\eta} = \rho g \pi R \; diag\left[\frac{J_1(\varepsilon_n)}{\beta_n \lambda_n^2}\right]_n$$

$$\boldsymbol{K}_{\eta\eta} = \rho g^2 \pi R \; diag\left[\frac{J_1(\varepsilon_n)}{\beta_n \lambda_n}\tanh(\lambda_n H)\right]_n$$

$$\boldsymbol{C}_{\eta\eta} = \boldsymbol{M}_{\eta\eta} \; diag[2h_n \omega_{sn}]_n$$

$$\boldsymbol{Q}_{\eta s} = \rho g \pi R \boldsymbol{W} \boldsymbol{R}_s$$

$$\boldsymbol{Q}_{\eta b} = \rho g \pi \; diag\left[-\frac{\alpha_n}{\cosh(\lambda_n H)}\right]_n \boldsymbol{R}_b$$

where h_n is critical damping ratio for the sloshing motion (value of 0.5% is used in this study); ω_{sn} is given in Eq. (24); $\alpha_n = \frac{1}{2}R^2\{J_1(\varepsilon_n)\}^2(\varepsilon_n^2 - 1)/\varepsilon_n^2$; and coefficients W_{nj} is in the nth row and jth column of matrix $\boldsymbol{W}$ are as follows

$$W_{n1} = -\lambda_n \tanh(\lambda_n H)$$

$$W_{n2} = -\lambda_n\left[H\tanh(\lambda_n H) + \frac{1}{\lambda_n}\left(\frac{1}{\cosh(\lambda_n H)} - 1\right)\right]$$

$$W_{n3} = -\lambda_n\left[\left(\frac{2}{\lambda_n^2} + H^2\right)\tanh(\lambda_n H) - \frac{2H}{\lambda_n}\right]$$

$$W_{n4} = -\lambda_n\left[\left(\frac{6H}{\lambda_n^2} + H^3\right)\tanh(\lambda_n H) + \frac{6}{\lambda_n^3}\left(\frac{1}{\cosh(\lambda_n H)} - 1\right) - \frac{3H^2}{\lambda_n}\right]$$

(A3) Shape functions in Eq. (26) and coefficients of added mass matrices in Eq. (27):

The shape function vectors in Eq. (26) are

$$\{\boldsymbol{N}_{\bar{U}_s}(z)\} = \boldsymbol{R}_s^T \boldsymbol{p}(z)$$

$$\{\boldsymbol{N}_{\bar{W}_b}(r)\} = \boldsymbol{R}_b^T \begin{Bmatrix} \cdots \\ J_1(\lambda_n r) \\ \cdots \end{Bmatrix}$$

The generalized added mass matrices in Eq. (27) are

$$\hat{\boldsymbol{M}}_{ss} = 2\rho\pi R^2 \boldsymbol{R}_s^T \left(\sum_{n=1}^{\infty} \frac{1}{\varepsilon_n^2 - 1} \hat{\boldsymbol{G}}_n \right) \boldsymbol{R}_s$$

$$\hat{\boldsymbol{M}}_{sb} = \rho\pi R^3 \boldsymbol{R}_s^T \hat{\boldsymbol{H}} \boldsymbol{R}_b$$

$$\hat{\boldsymbol{M}}_{bb} = \rho\pi \boldsymbol{R}_b^T diag\left[\frac{\alpha_n}{\lambda_n} \tanh(\lambda_n H) \right]_n \boldsymbol{R}_b$$

where

$$\hat{\boldsymbol{H}} = \left[\ldots, \frac{J_1(\varepsilon_n)}{R^2} \int_0^H \boldsymbol{p}(z) \tilde{E}_n(z) dz, \ldots \right]$$

$$\hat{\boldsymbol{G}}_n = \int_0^H \boldsymbol{p}(z) \{\boldsymbol{E}_n(z)\}^T dz$$

in which $\hat{\boldsymbol{G}}_n$ is a symmetric matrix with coefficients of $\hat{G}_{nij}$ in its ith row and jth column as

$$\hat{G}_{n11} = H - \frac{1}{\lambda_n} \tanh(\lambda_n H)$$

$$\hat{G}_{n12} = \frac{H^2}{2} - \frac{H}{\lambda_n} \tanh(\lambda_n H) + \frac{1}{\lambda_n^2} \left(1 - \frac{1}{\cosh(\lambda_n H)} \right)$$

$$\hat{G}_{n13} = \frac{H^3}{3} + \frac{2H}{\lambda_n^2} - \left(\frac{H^2}{\lambda_n} + \frac{2}{\lambda_n^3} \right) \tanh(\lambda_n H)$$

$$\hat{G}_{n14} = \frac{H^4}{4} + \frac{3H^2}{\lambda_n^2} - \left(\frac{H^3}{\lambda_n} + \frac{6H}{\lambda_n^3} \right) \tanh(\lambda_n H) + \frac{6}{\lambda_n^4} \left(1 - \frac{1}{\cosh(\lambda_n H)} \right)$$

$$\hat{G}_{n22} = \frac{H^3}{3} - \frac{H}{\cosh(\lambda_n H)} \left(\frac{H}{\lambda_n} \sinh(\lambda_n H) - \frac{\cosh(\lambda_n H)}{\lambda_n^2} + \frac{1}{\lambda_n^2} \right) + \frac{1}{\lambda_n^2} \frac{1}{\cosh(\lambda_n H)} \left(\frac{1}{\lambda_n} \sinh(\lambda_n H) - H \right)$$

$$\hat{G}_{n23} = \frac{H^4}{4} + \frac{H^2}{\lambda_n^2} - \left(H^2 + \frac{2}{\lambda_n^2} \right) \left(\frac{H}{\lambda_n} \tanh(\lambda_n H) - \frac{1}{\lambda_n^2} + \frac{1}{\lambda_n^2 \cosh(\lambda_n H)} \right)$$

$$\hat{G}_{n24} = \frac{H^5}{5} + \frac{2H^3}{\lambda_n^2} - \left(H^3 + \frac{6H}{\lambda_n^2}\right)\left(\frac{H}{\lambda_n}\tanh(\lambda_n H) - \frac{1}{\lambda_n^2} + \frac{1}{\lambda_n^2\cosh(\lambda_n H)}\right) + \frac{6}{\lambda_n^4}\left(\frac{\tanh(\lambda_n H)}{\lambda_n} - \frac{H}{\cosh(\lambda_n H)}\right)$$

$$\hat{G}_{n33} = \frac{H^5}{5} + \frac{2H^3}{3\lambda_n^2} - \left(H^2 + \frac{2}{\lambda_n^2}\right)\left(\left(\frac{H^2}{\lambda_n} + \frac{2}{\lambda_n^3}\right)\tanh(\lambda_n H) - \frac{2H}{\lambda_n^2}\right)$$

$$\hat{G}_{n34} = \frac{H^6}{6} + \frac{3H^4}{2\lambda_n^2} - \left(H^3 + \frac{6H}{\lambda_n^2}\right)\left(\left(\frac{H^2}{\lambda_n} + \frac{2}{\lambda_n^3}\right)\tanh(\lambda_n H) - \frac{2H}{\lambda_n^2}\right) + \frac{6}{\lambda_n^4}\left(\frac{2}{\lambda_n^2} - \left(H^2 + \frac{2}{\lambda_n^2}\right)\frac{H}{\cosh(\lambda_n H)}\right)$$

$$\hat{G}_{n44} = \frac{H^7}{7} + \frac{6H^5}{5\lambda_n^2} - \left(H^3 + \frac{6H}{\lambda_n^2}\right)\left(\left(\frac{H^3}{\lambda_n} + \frac{6H}{\lambda_n^3}\right)\tanh(\lambda_n H) - \frac{3H^2}{\lambda_n^2} - \frac{6}{\lambda_n^4} + \frac{6}{\lambda_n^4}\frac{1}{\cosh(\lambda_n H)}\right)$$

$$+ \frac{6}{\lambda_n^4}\left(\frac{6}{\lambda_n^3}\tanh(\lambda_n H) - \left(H^3 + \frac{6H}{\lambda_n^2}\right)\frac{1}{\cosh(\lambda_n H)}\right)$$

and coefficients $\hat{H}_{jn}$ in the jth row and nth column of matrix $\hat{\boldsymbol{H}}$ are given by

$$\hat{H}_{1n} = \frac{J_1(\varepsilon_n)}{\varepsilon_n^2}\left(\frac{1}{\cosh(\lambda_n H)} - 1\right)$$

$$\hat{H}_{2n} = \frac{J_1(\varepsilon_n)}{\varepsilon_n^2}\left(\frac{H}{\cosh(\lambda_n H)} - \frac{1}{\lambda_n}\tanh(\lambda_n H)\right)$$

$$\hat{H}_{3n} = \frac{J_1(\varepsilon_n)}{\varepsilon_n^2}\left(\frac{1}{\cosh(\lambda_n H)}\left(H^2 + \frac{2}{\lambda_n^2}\right) - \frac{2}{\lambda_n^2}\right)$$

$$\hat{H}_{4n} = \frac{J_1(\varepsilon_n)}{\varepsilon_n^2}\frac{1}{\cosh(\lambda_n H)}\left(H^3 + \frac{6H}{\lambda_n^2} - \frac{6}{\lambda_n^3}\sinh(\lambda_n H)\right)$$

(A4) Infinite elements for far field region :

The horizontal, vertical and corner axisymmetric infinite elements used for the far field region in this study are briefly described (Yun *et al.* 1995). The number of nodes for horizontal and vertical infinite elements is 3 along the interface with the finite element, while it is 1 for the corner infinite element as in Figs. A1-A3. The displacement fields for the infinite elements are obtained by using the approximate wave functions for the primary, shear and Rayleigh waves as:

$$\boldsymbol{u}(r, z;\omega) = \sum_{j=1}^{N}\sum_{m=1}^{M}\tilde{N}_{jm}(r, z;\omega)\boldsymbol{b}_{jm}(\omega)$$

where N is the number of nodes for horizontal and vertical infinite elements, while it is the number of horizontal wave functions in the corner infinite element; and M is the number of wave functions included in the formulation of the infinite element. The shape functions $\tilde{N}_{jm}$ are expressed as:

$$\tilde{N}_{jm}(r, z;\omega) = \begin{cases} L_j(\eta)f_m(\xi;\omega) & \text{for HIE} \\ f_j(\xi;\omega)g_m(\zeta;\omega) & \text{for CIE} \\ L_j(\eta)g_m(\zeta;\omega) & \text{for VIE} \end{cases}$$

and $\boldsymbol{b}_{jm}(\omega)$ is the generalized coordinate associated with $\tilde{N}_{jm}(r, z;\omega)$; $L_j(\eta)$ is the Lagrange interpolation function associated with node j; $f_j(\xi;\omega)$ and $g_m(\zeta;\omega)$ are wave functions obtained from the function spaces consisting of the approximate wave functions for the primary, shear and Rayleigh waves as follows

$$f_m(\xi;\omega) \in \{e^{-(\beta + ik_s r_0)\xi}, e^{-(\beta + ik_p r_0)\xi}, \{e^{-(\alpha + ik_R r_0)\xi}\}_{R=1}^{N_R}\}$$

$$g_m(\zeta;\omega) \in \{e^{-(\beta + ik_s)\zeta}, e^{-(\beta + ik_p)\zeta}, \{e^{-\mu_{sR}\zeta}, e^{-\mu_{pR}\zeta}\}_{R=1}^{N_R}\}$$

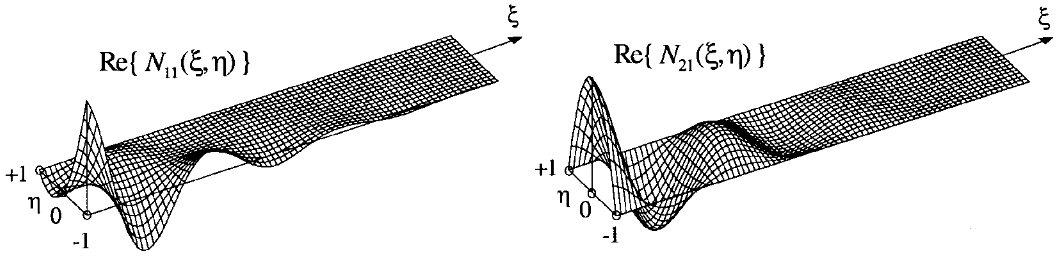

Fig. A1 Shape functions for horizontal element ($N_{jm} = L_j(\eta)f_m(\xi)$)

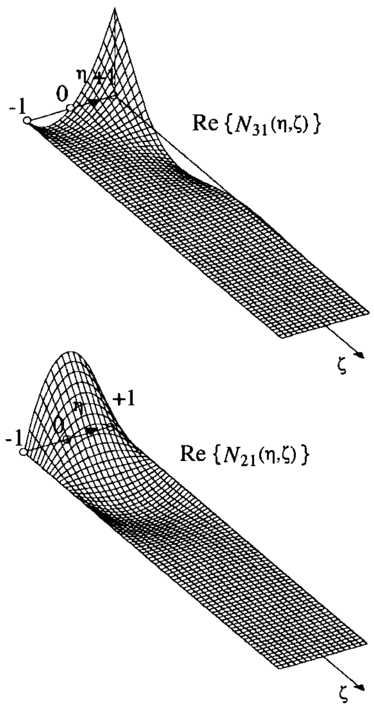

Fig. A2 Shape functions for vertical element ($N_{jm} = L_j(\eta)g_m(\zeta)$)

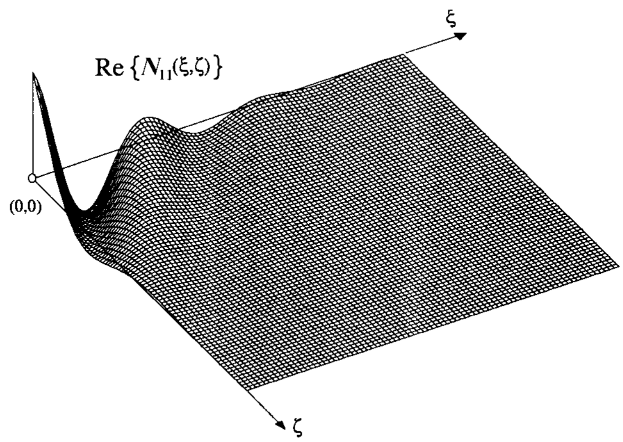

Fig. A3 Shape function for a corner element ($N_{jm} = f_j(\xi)\, g_m(\zeta)$)

in which the functions have unit value at $\xi = 0$ or $\zeta = 0$; α and β are positive constants, which are related to the geometric attenuation for the surface and body waves; r_0 is the horizontal distance from the origin of the global coordinates to the horizontal infinite element; $k_s(\omega)$, $k_p(\omega)$, and $k_R(\omega)$ are the wave numbers of the shear, primary, and Rayleigh waves; μ_{sR} and μ_{pR} can be obtained as

$$\mu_{sR} = \sqrt{k_R^2 - k_{sl}^2}, \quad \mu_{pR} = \sqrt{k_R^2 - k_{pl}^2}$$

$$k_{sl} = \omega / \sqrt{(\lambda_l + 2G_l)/\rho_l}, \, k_{pl} = \omega / \sqrt{G_l/\rho_l}$$

and λ_l, G_l, and ρ_l are the material properties of the l-th layer. Real parts of the typical shape functions for the horizontal, vertical, and corner infinite elements are shown in Figs. A1, A2, and A3.